Design Study for a High-Accuracy Three-Axis Test Table

Louis A. DeMore,* Robert A. Peterson,† Louis B. Conley,‡ Howard H. Havliscek,§
Nikos P. Andrianos,¶ David H. Ditto,** and Joseph Profeta III††
Contraves Goerz Corporation, Pittsburgh, Pennsylvania

A comprehensive study of principal features affecting the design and fabrication of a high-accuracy three-axis test table was completed. The improved, third-generation motion simulation test equipment is intended for advanced guidance and navigation component testing. The work produced analytical models for predicting the table's overall pointing accuracy and rate stability. The subsystem performance requirements support more than an order-of-magnitude improvement over present state-of-the-art pointing accuracy and rate stability.

Introduction

THIS study was initiated with the following four general design goals:

1) The motion simulator shall accommodate a test package that weighs 100 lb, occupies a 12-in. cube, and requires 100 electrical connections.

2) The simulator shall be capable of rotating the test package continuously and simultaneously about each of the mutually perpendicular axes; the outermost axis shall lie in the horizontal plane.

3) The simulator shall be capable of positioning the test package to within 0.1 arcsec of any desired pointing position.

4) The simulator shall be capable of rotating the test package about any of its axes with a rate stability of less than 1 ppm over the dynamic range of ± 0.001–200 deg/s.

The last two goals—pointing accuracy and rate stability—represent improvements over the present state-of-the-art for inertial grade test tables. Table 1 lists data for several of the principal parameters contributing to pointing error for the conventional mechanical and air bearing systems. A pointing error figure of merit is given as simply the root sum square of the contributing errors. Table 2 lists the rate stability performance for the two types. The instantaneous rate stability and position jitter values were measured, and the average rate stability is calculated from the instantaneous position jitter. At least one-order-of-magnitude improvement is needed for both pointing and rate stability performance to meet the design goals.

The subsystems evaluated during the study were: 1) gimbal configuration/structural consideration, 2) bearing configuration, 3) axis sensors, 4) actuators, 5) signal transmission to test package, and 6) instrumentation and control.

Presented as Paper 85-1893 at the AIAA Guidance, Navigation, and Control Conference, Snowmass, CO, Aug. 19–21, 1985; received Dec. 13, 1985; revision submitted May 2, 1986.

*Operations Manager, Motion Simulation Systems. Member AIAA.
†Group Vice President, Inertial Guidance Test Systems. Member AIAA.
‡Senior Engineer, Motion Simulation Systems.
§Engineering Manager, Research and Development.
¶Senior Engineer, Research and Development.
**Chief Electrical Engineer, Military Programs. Member AIAA.
††Associate Engineer, Motion Simulation Systems.

The principal analytical tools used to assess the subsystem evaluations were the composite pointing error model and the dynamic rate stability model.

Error Models

Two error models were developed to predict both static and dynamic errors. The first model is based on rigid-body kinematics and calculates the static-body positioning errors. The second model is a dynamic simulation of the servo system and, with the use of an on-line autocorrelator, calculates the actual position and rate error variances as well as the estimated rate error variance.

Pointing error is defined as the difference between the intended (true) angle and the actual angle of a unit vector attached to the innermost gimbal of the simulator for all possible pointing directions. See Fig. 1.

The orthogonal unit vector set $X=(X_1, X_2, X_3)$ represents the original, fixed, coordinate reference frame; the vector η_0 is an arbitrary unit vector attached to the innermost gimbal.

A series of perfect yaw, pitch, and roll rotations through the angle set $\Omega=(\alpha, \beta, \gamma)$ will move the vector to the intended true vector η'; i.e., $\eta'=R_0(\Omega)\eta_0$, where $R_0(\Omega)$ is the appropriate direction cosine matrix. The same angular rotation in the presence of individual simulator errors, represented by the error set $E=(K, w, \epsilon)$, will move the vector to its actual location, η''. That is, $\eta''=R'(\Omega,E)\eta_0$.

The angle $\Delta\Phi$ between η' and η'' is the pointing error for the particular initial pointing direction represented by η_0. Since η_0, η', and η'' are unit vectors,

$$\Delta\Phi = |\eta'' - \eta'| = \Delta\eta \tag{1}$$

where

$$\Delta\eta^2 = \eta_0^T \delta R^T \delta R \eta_0$$

$$\delta R \triangleq R_0 - R'$$

Figure 2 is a pictorial sketch of the individual simulator errors included in the set $[K,w,\epsilon]$. These are the peak orthogonality errors between the mutually orthogonal axes, $K=(\pm K_1, \pm K_2, \pm K_3)$; the peak axis wobble errors, $w=(\pm w_1, \pm w_2, \pm w_3)$; and the peak axis encoder errors, $\epsilon=(\pm\epsilon_1, \pm\epsilon_2, \pm\epsilon_3)$.

The pointing error defined by Eq. (1) is a function of not only the angles of rotation and individual simulator errors, but also a function of the pointing direction. To avoid the dependence on pointing direction, the maximum average

pointing error was used. The pointing error is defined as the average of the error in each of the three mutually orthogonal, original, fixed coordinates. The mean square error is

$$\bar{\delta}^2 = \tfrac{1}{3} \sum_{i=1}^{3} \Delta X_i^2 \tag{2}$$

where

$$\Delta X_i^2 = [\delta R^T \delta R]_{ii}$$

or

$$\bar{\delta}^2 = \tfrac{1}{3} \mathrm{tr}\,[\delta R^T \delta R] \tag{3}$$

The maximum average pointing error is the maximum of Eq. (3) over the range of gimbal angles and individual peak simulator errors, i.e.,

$$\bar{\delta}_{\max} \triangleq [\tfrac{1}{3} \max_{\Omega, E} \{\mathrm{tr}(\delta R^T \delta R\}]^{1/2} \tag{4}$$

A computational algorithm was developed to compute the quantity in Eq. (4). The worst-case combination of the orientation and the signed individual simulator errors were chosen to ensure that the maximum pointing error was calculated. Table 3 gives the results of the calculations for encoding, wobble, and orthogonality errors. The value of 0.016 was used to measure the sensitivity of the pointing error to the individual errors. The data showed the pointing error is at least 60% more sensitive to the orthogonality error than to either the encoder or wobble errors. Also, this is the error budget for each of the individual errors in order for the maximum average pointing error to be less than 0.1 arcsec.

Figure 3 is a graphical presentation of the pointing error sensitivity to the orthogonality error over the range of 0.005–0.025 arcsec for a fixed encoder error of 0.01 arcsec and wobble errors of 0.01, 0.02, and 0.03 arcsec. In this small, linear range, the sensitivity of the pointing error to orthogonality error is approximately 3.5 arcsec/arcsec.

Rate stability in fraction is expressed in terms of variances of the rate process, i.e.,

$$\left[\frac{\mathrm{var}\{\dot{\theta}(t)\}}{\dot{\theta}_0^2}\right]^{1/2} = \left[\frac{E\{[\dot{\theta}(t) - \dot{\theta}_0(t)]^2\}}{\dot{\theta}_0^2}\right]^{1/2} \tag{5}$$

and

$$\dot{\theta}_0(t) = E\{\dot{\theta}(t)\}$$

where

$E\{\cdot\} \triangleq$ mean value operator

$\dot{\theta}(t) \triangleq$ rate process

$\dot{\theta}_0(t) \triangleq$ rate mean value

In this study, the rate process is described in two ways: 1) as an instantaneous time-evolving stochastic process $\dot{\theta}(t)$, and 2) as a sampled process taken over a fixed, spatial interval $\tilde{\dot{\theta}}(t)$. Both are stochastic processes; the latter approches the former as the fixed observation interval approaches zero. The variance of the former is termed "instantaneous" rate stability, while the variance of the latter is termed "average" rate stability. The "average" rate stability is directly related to the variance of the "instantaneous" position process $\theta(t)$, which is the time integral of the instantanteous rate process. The "average" rate stability in fraction is given by

$$\left[\frac{\mathrm{var}\{\tilde{\dot{\theta}}(t)\}}{\dot{\theta}_0^2}\right]^{1/2} = \left[\frac{\mathrm{var}\{\theta(t)\}}{\theta_0^2}\right]^{1/2} \tag{6}$$

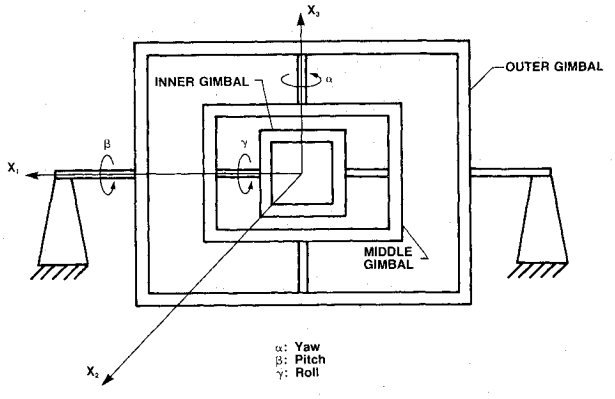

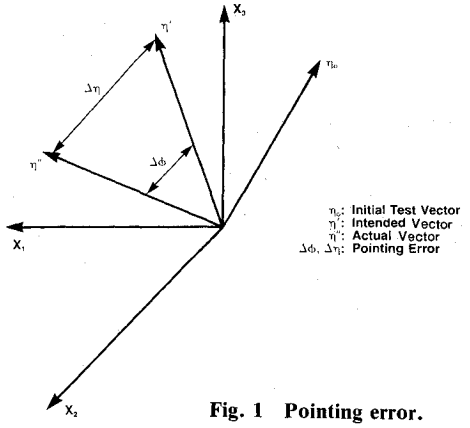

Fig. 1 Pointing error.

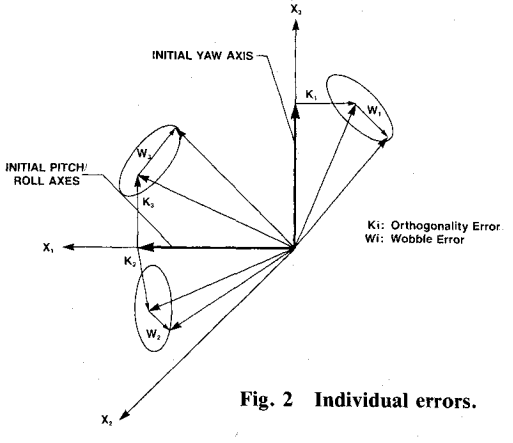

Fig. 2 Individual errors.

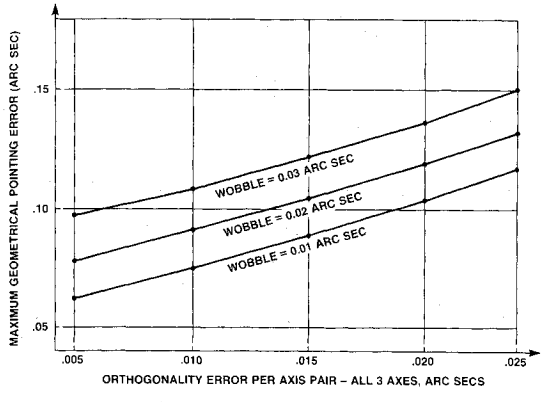

Fig. 3 Pointing error sensitivity to orthogonality error (maximum encoder error fixed at 0.02 arcsec).

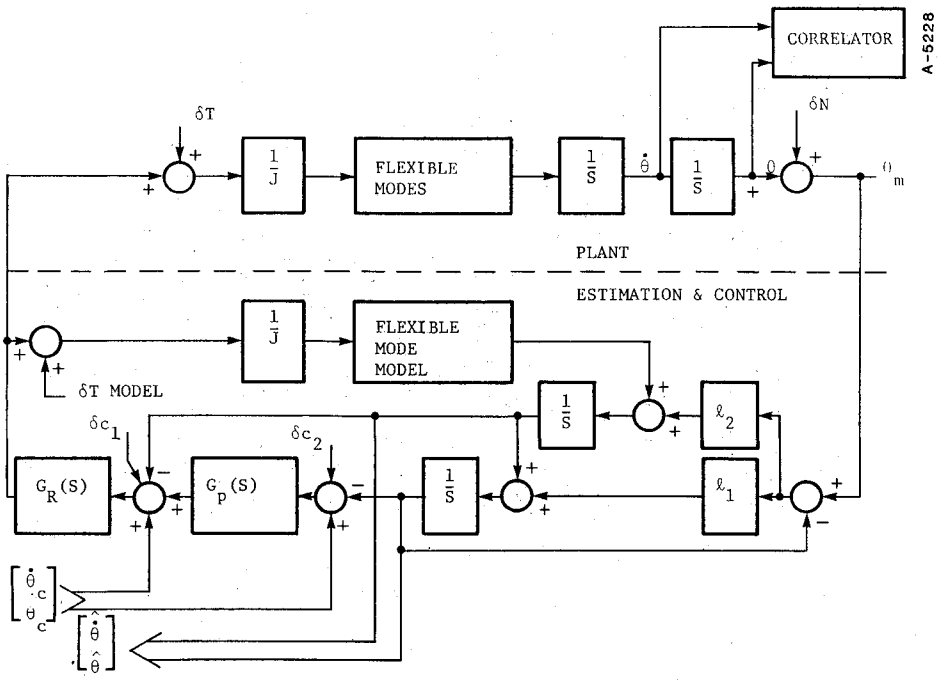

Fig. 4 Axis servo system.

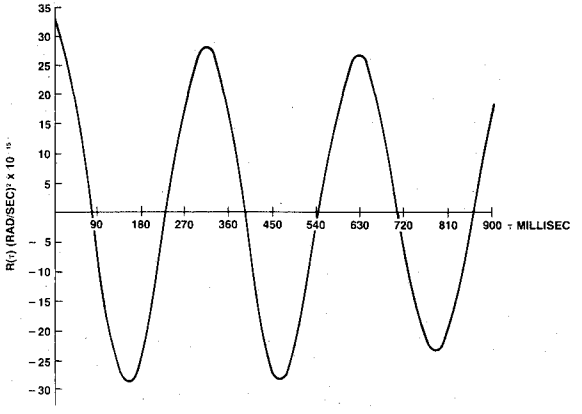

Fig. 5 Autocorrelation function of rate process with servo system rating at 1 rad/s.

where

$$\theta(t) = \int_0^t \dot{\theta}(t)\,dt$$

$\theta_0 \triangleq$ fixed observation interval

$\theta(t) \triangleq$ position process

Equations (5) and (6), for the instantaneous and averaged rate processes, respectively, are used to define rate stability.

Figure 4 is a block diagram of a typical axis servo system. The servo system consists of 1) a simple, two-stage, state estimator, 2) a rate servo loop using the estimate of rate as the feedback variable, and 3) a position servo loop using the estimate of position as the feedback variable. Command noise δc is included to represent quantization and roundoff error in the control algorithm. The torque disturbance δT represents both the periodic and random residuals in the actuator system. The sensor error δN represents both the periodic and random residuals in the position measurement system. The characteristics of these error terms in the model are:

δc = band-limited white noise with finite variance, ϕ_1^2 (7)

Table 1 Selected test data for multiaxis simulators

	Air bearing system	Mechanical bearing system
Wobble, arcsec rms		
Inner	0.33	0.45
Middle	0.25	0.5
Outer	0.47	0.6
Orthogonality, arcsec		
Inner/middle	0.4	2.1
Middle/outer	0.4	0.9
Position accuracy, arcsec rms		
Inner	0.85	0.46
Middle	0.64	0.74
Outer	0.52	0.98
Pointing error, arcsec rms	1.45	2.78

Table 2 Rate stability comparisons

	Air bearing system	Mechanical bearing system
Instantaneous rate stability at 10 deg/s, ppm rms	9×10^{3}	3×10^{4}
Instantaneous position jitter at 0.001 deg/s, deg rms	3×10^{-5}	1×10^{-4}
Average rate stability at 0.001 deg/s over 1-deg interval, ppm rms	30	100

Table 3 Computational results of pointing error

Error source per axis, arcsec			Maximum average pointing error, arcsec
Encoder	Orthogonality	Wobble	
1.0	0	0	2.2
0	1.0	0	3.5
0	0	1.0	2.2
1.0	1.0	1.0	6.4
0.016	0.016	0.016	0.1

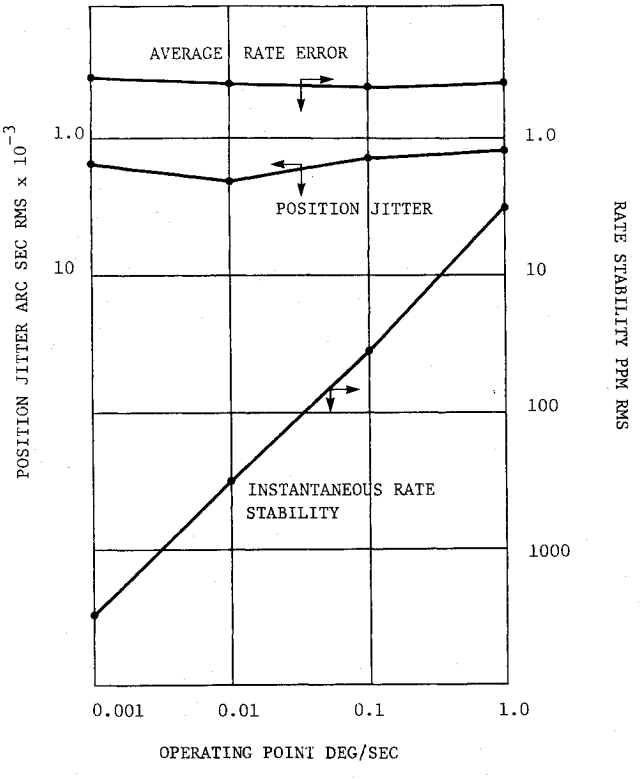

Fig. 6 Rate and position stability vs operating point.

$$\delta T = B\sin(m\dot{\theta}t + \psi_1) + N_2(t) \tag{8}$$

where B and m are constants, $\psi_1 \triangleq$ random phase angle, and $N_2(t) \triangleq$ band-limited white noise with finite variance, ϕ_2^2.

$$\delta N = A_0\sin(2\dot{\theta}t + \psi_2) + [A_1\sin(\dot{\theta}t + \psi_3) + A_2\sin(16\dot{\theta}t + \psi_3)] + [C_1\sin(360\dot{\theta}t + \psi_2) + C_2\sin(720\dot{\theta}t + \psi_2) + C_3\sin(1440\dot{\theta} + \psi_2)] + N_3(t) \tag{9}$$

where A_i and C_i are constants, ψ_2 and ψ_3 are random phase angles, and $N_3(t) \triangleq$ band-limited white noise with finite variance, ϕ_3^2.

A dynamic simulation of the servo system with the individual error terms defined by Eqs. (7-9) was constructed. Under these perturbed conditions, the autocorrelation functions of both the instantaneous rate and position processes were computed. Figure 5 shows a typical plot of the computed autocorrelation function for the rate process after reaching a steady-state operating rate of 1 rad/s. The total correlation interval was 1 s and the computation interval was 1 ms. Figure 6 shows the rate stability and square root of the position variance (termed position jitter) as functions of the operating point. Table 4 lists the errors used to generate the data in Fig. 6. It also represents the individual error budgets for the actuator, measurement, and command systems to achieve the overall rate stability goals.

Mechanical Structure

Figure 7 shows the final mechanical configuration selected after extensive stress and thermal deflection analyses. This structure, which will provide the mechanical support for all components, consists of the base, the three gimbals, and the test package mounting fixture.

The rotating gimbals are supported by a stationary base assembly, which provides a mounting for the outer axis bearings. Granite was chosen for the base material because of its inherently high structural damping characteristics, large thermal inertia, and a low coefficient of expansion that minimizes dimensional changes due to temperature variations. Furthermore, since it has been aged and stress-relieved over millions of years, granite is extremely insensitive to dimensional creep caused by prolonged stress or temperature change.

Table 4 Error budgets

System	Error
Actuator system	
B: Peak torque ripple, ft-lb	5×10^{-5}
ϕ_2: Broadband torque noise, ft-lb-rms	5×10^{-5}
Measurement system	
A_0, A_1: Peak coarse position error, arcsec	0.01
C_i, A_2: Peak fine harmonics, arcsec	0.01
ϕ_3: Broadband sensor noise, arcsec rms	0.01
Command system	
ϕ_1: Broadband command noise, arcsec rms	0.01

The gimbals transfer loads from the test package to the base, and from the base back to the test package. The main requirement for the gimbals is stability. They must not cause any significant rotations of the test package under any condition (i.e., the gimbal deflections must be uniform under all conditions). The selected design uses a lightweight shell construction for maximum rigidity and dimensional stability.

The inner gimbal is configured as a sphere with a square hole for mounting the test load. The middle gimbal is configured as an oval with a hollow spherical inside surface, and the outer gimbal is configured as a sphere with a hollow, discus-shaped inside surface. Both the outer and middle gimbals may be fabricated in two halves that can be bolted and pinned together to facilitate assemblying the internal gimbal and bearings. The outer gimbal, similar to the middle gimbal, is equipped with access holes for mounting and servicing the test load. The inner and middle gimbals are supported by bearings housed in the middle and outer gimbals, respectively. The outer gimbal is supported by bearings housed in pillow blocks on the support base.

Double-walled shell construction was selected to more efficiently achieve high structural stiffness. Both outer and middle gimbals have a shell separation distance of 6 in. The outer structure is 60-in. o.d. (48-in. i.d.), whereas the middle structure is 40-in. o.d. (28-in. i.d.). The inner structure is 26 in. o.d. with a 12-in.-square inside surface cross-section. A finite element model (FEM) of the three-axis gimbal set using the ANSYS® (trademark of Swanson Analysis Systems Inc., Houston, Pennsylvania) laminated shell elements (see Fig. 8) was constructed. The mesh contains approximately 1400 elements, with a solution wavefront of 430. With this model, test package rotations with respect to the base, due to gravitational and thermal-induced gimbal deflections were calculated.

The gravity response of the test package is determined for two separate unbalanced conditions. The first case corresponds to a test package center-of-gravity (c.g.) displacement from the intersection of gimbal axes to produce an imbalance of 1 in.-lb (1 lb at $Z = 1$ in.) This case presupposes that the 100-lb test package and mounting fixture are counterbalanced to within 1 in.-lb. The gimbals are rotated in a 1-g field, and test package rotations are observed; peaks occur when gravity is in line with the X or Y axis. This results in a maximum angular deflection of 0.002 arcsec. The second case assumes that the test package is initally 100 in.-lb unbalanced (100 lb offset by 1 in.), and static balance is achieved by adding counterweights to the inner and middle gimbals. Three cases for this type of nonsymmetric balancing, designated by X, Y, and Z balances, are illustrated in Fig. 9.

The individual nonsymmetric balance cases assume that the 100-lb test package c.g. is located at either X, Y, or $Z = +1$ in. Counterbalance is provided by placing proper weights at

points A and B on the inner structure for the X-balance case, at C and D on the inner structure for the Y-balance case, or at D and E on the inner strucure for the Z-balance case. Gravity-induced test package rotations for the X-balance case are insignificant, while the Y-balance case produces 0.027 arcsec maximum and the Z-balance case produces 0.03 arcsec maximum.

The ANSYS thermal analysis was conducted with a thermal FEM of the identical geometry as the structural FEM used in the gravity response analysis. The boundary condition assumed for the thermal response is natural convection to ambient air at 70°F. The natural convection surfaces selected are the outside surfaces of the outer and middle structures. Other surfaces are assumed adiabatic.

The nominal distribution assumes that heat enters the system equally at the shaft centers; this model simulates heat added by the bearing system and torque motors. Two variations about this nominal distribution were studied. The first case, designated the on-axis unbalanced condition, imposes a ±10% variation on the heating, yet retains the shaft center location. The second case, designated as the off-axis unbalanced heating, corresponds to specifying heating ($Q=1$ W) at a single point on the outer structure adjacent to the outer axis. Heating at other parts of the structure is neglected. For both the nominal case and the on-axis unbalanced case, the test package motion is strictly translational. For the last case, a test package rotation of less than 0.01 arcsec was calculated.

The total peak power added to the structure during operation is due to the torque motor and magnetic suspension system. The primary effect of this added heat is represented by either the nominal or on-axis unbalanced cases, which result in no test package rotation. The off-balance heating load, however, must be kept to less than 1 W (less than 2% of the total power consumption) to have an insignificant effect on the test package rotation.

Along with aluminum, advanced composites were studied to determine their susceptibility to gravitational and thermal loadings. The carbon fiber reinforced plastic (CFRP) has extremely high stiffness-to-weight and strength-to-weight ratios. The material properties for the three-axis gimbal set were changed in the model to represent the CFRP; and the FEM structural analysis was then repeated. For the thermal loading cases, the deflections were the same as the aluminum. For the gravitational loading cases, the 1 in.-lb test package/fixture unbalanced case and the 100 in.-lb counterweight balanced case showed significant reductions in test package rotations with the CFRP. Table 5 summarizes the gravity and thermal deflections for both aluminum and CFRP.

Bearings

During the initial phase of the design study, the following four types of gimbal axes bearing systems were analyzed: mechanical ball bearings, hydrostatic oil bearings, aerostatic air bearings, and active magnetic bearings.

However, the mechanical ball bearings were eliminated from consideration due to large wobble with a significant random component and high stiction and running friction. The hydrostatic oil bearing was eliminated because of the high viscous friction and a particularly complex support system. Thus, only the air and magnetic bearings were analyzed in detail. The criteria used to compare the two systems were: wobble, friction (starting and running), axes orthogonality, stiffness, reliability, and support-system simplicity.

An air bearing can be defined as two conforming surfaces of rotational symmetry separated by a film of fluid. Externally pressurized bearings are used in precision spindles requiring low or reversible speed. A pressurized medium is fed at the supply pressure P_s into the bearing (see Fig. 10), a control element expands it to pressure condition P_r, and it decreases to the pressure condition P_a at the exhaust edge. The pressure drop (P_s-P_r) permits a mass flow (Q_{in}), to pass through the control element. The pressure drop (P_r-P_a) across the film produces the mass flow (Q_{out}). This steady-state condition establishes the relationship between the film thickness h and the load capacity W. A typical plot of load vs film thickness is shown in Fig. 11. The inflection point of the curve is the point of maximum stiffness, and is used as the nominal operating point.

The air bearing stability and performance is completely determined by the aerostatic and geometric conditions of the

Table 5 Predicted gravity and thermal response for double-walled construction

Loading	Description	Test package rotation, Al, arcsec	Test package rotation, CFRP, arcsec
Gravity	Test package and fixture unbalanced at 1 in.-lb	<0.002	0.0013
Gravity	Test package initially unbalanced (100 in.-lb) and balanced by counterweights	<0.03	0.01
Thermal	Off-axis unbalanced heating at outer axis bearing only (1 W)	<0.01	0.01

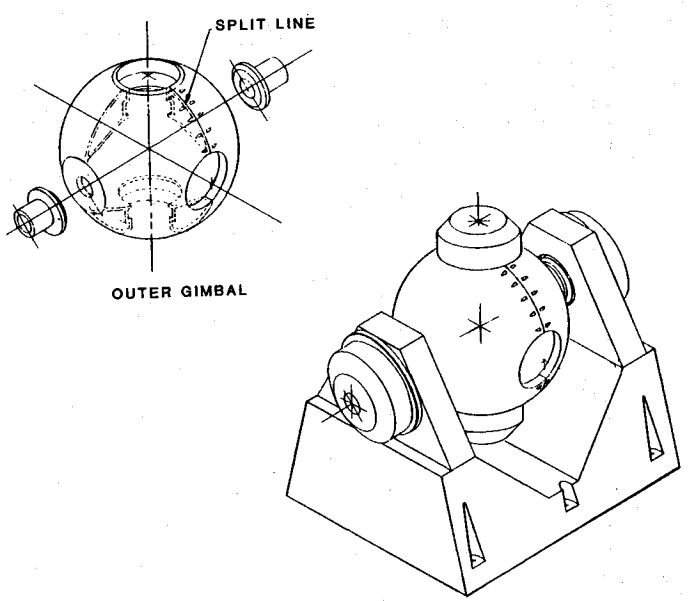

Fig. 7 Conceptual drawing of high-accuracy three-axis test table.

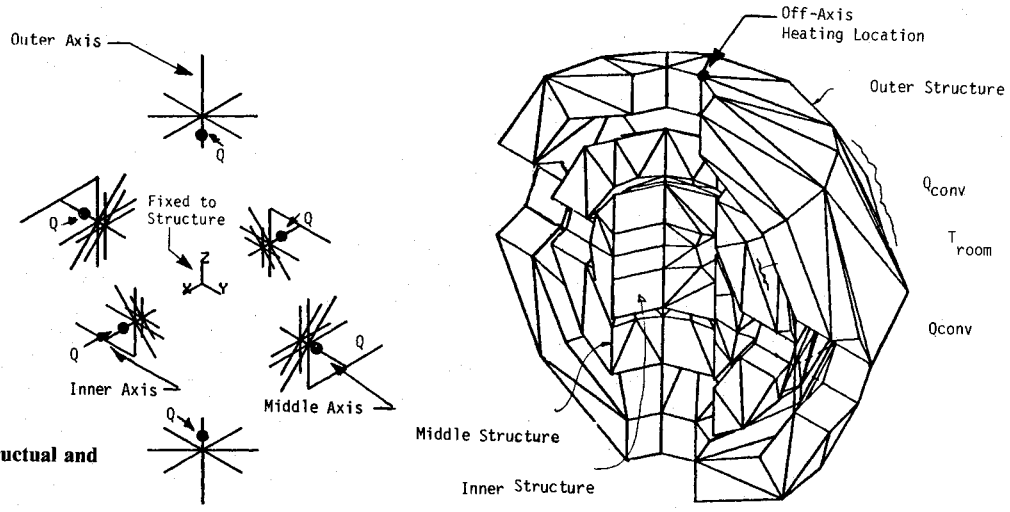

Fig. 8 Finite element model for structual and thermal analysis.

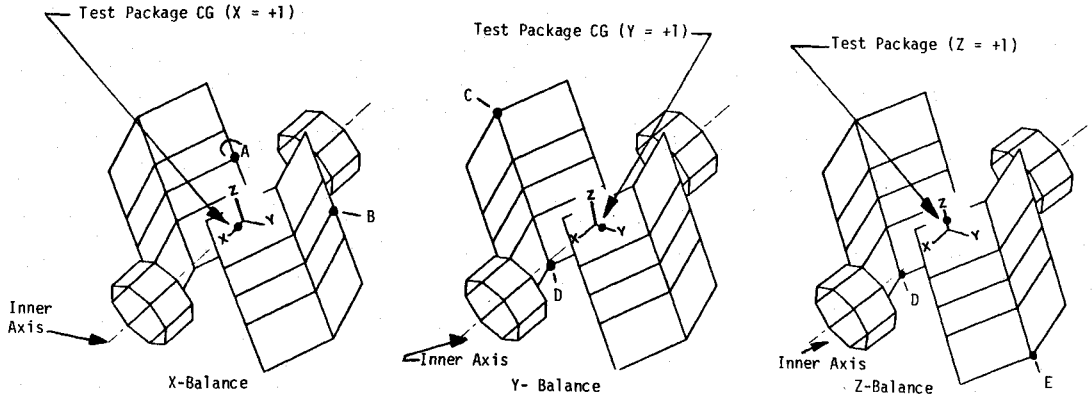

Fig. 9 Nonsymmetric balance for gravity response.

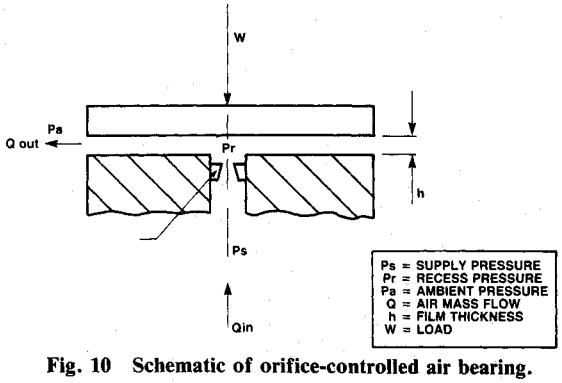

Fig. 10 Schematic of orifice-controlled air bearing.

bearing; there is no active feedback compensation for the system once manufactured. When designed and fabricated properly, the bearings exhibit good stability margin with high thrust and radial stiffness ($\sim 10 \times 10^6$ lb/in.) and low wobble (~ 0.5 arcsec). They are extremely reliable and simple to operate and support; an air compressor with proper filtration and drying is all that is necessary. Air turbulent torques provide the bulk of the unwanted torque disturbance; there is no coulomb friction and very low viscous friction [0.1 in.-lb/(rad/s)]. Since the system is basically passive, thre are no provisions for adjusting the axis alignment to achieve orthogonality requirements in multiaxis systems.

The active magnetic bearing consists of a ferromagnetic laminated rotor suspended in the magnetic flux of electromagnets fixed to the stator. In the general case for an axis employing both thrust and radial bearings, the bearing system must apply magnetic forces along five independent axes. Figure 12 depicts the five controlled axes: two perpendicular axes at each shaft end, and a fifth axis parallel to the shaft's rotational axis.

Active feedback control systems are employed to both stabilize and accurately position the rotor in space. The control systems are typically type 3 servos employing a position sensor in the outer loop. The position sensor is usually an inductive type (magnetic coils and reference ring) sensing impedance (airgap) variations.

Servo quality and feedback control drift are the primary factors affecting rotor position, axis wobble, and orthogonality. Reference ring defects (eccentricities, etc.) are the greatest contributors to rotor orientation error. With proper manufacturing and calibration, this error could be reduced to produce an axis wobble of less than 0.04 arcsec, and perhaps even 0.02 arcsec. The alignment of consecutive axes can be adjusted to maintain orthogonality to within 0.01 arcsec. The control system continually maintains and regulates the suspension; the control-loop drift, however, will cause errors of its own. Conventional electronic hardware drift can be limited to 5 μV/°C. If the electronics temperature rise is kept below 20°C, the drift will be less than 0.04 μin. The resulting wobble and orthogonality errors for a typical axis will be two orders of magnitude less than the misalignment values.

The disturbance torques produced by the bearing at low speed are predominantly due to hysteresis iron losses. A special test was set up to measure the disturbance torques for a conventional magnetic bearing at low speed and then to project these findings to total torque disturbance per axis. Figure 13 shows the predicted bearing torque vs displacement for the

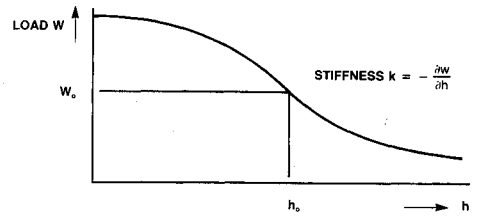

Fig. 11 Load vs film thickness for air bearing.

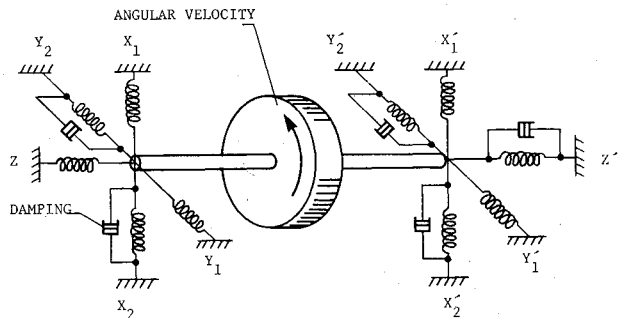

Fig. 12 Active magnetic bearing model, springs represent electromagnets.

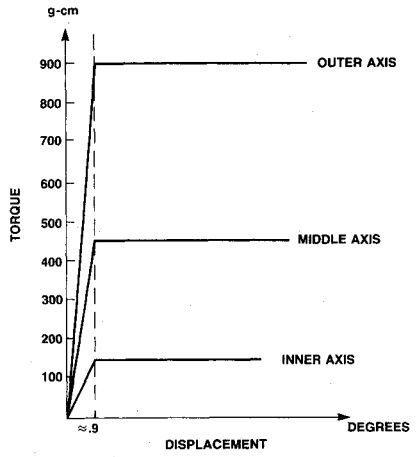

Fig. 13 Torque vs displacement in active magnetic bearing system.

inner, middle, and outer axes. The torque is independent of rate, constant beyond a certain threshold and quite linear for small displacements about zero (up to twice the airgap value). The expected running torque for the outer axis is approximately 0.8 in.-lb.

Since the bearing system is essentially an integral-type servo loop, the bearing stiffness if governed by the typical torque rejection curve. This is a function of excitation (torque disturbance) frequency. Figure 14 is a typical stiffness curve. For low frequencies, the stiffness is dominated by the control system dynamics; the high frequencies are dominated by the axis inertia or mass. For a system typical of the inner axis (inertial weight of approximately 200 lb), the servo natural frequency is approxiamtely 100 Hz. The midband (worst case) stiffness is expected to be on the order of 0.1×10^6 lb/in., while the low-frequency stiffness (less than 1 Hz) will be greater than 2×10^6 lb/in.

Table 6 presents a comparison of the air bearing and magnetic bearing systems. Only the first three characteristics—wobble, orthogonality, and friction—are important to the overall test table performance.

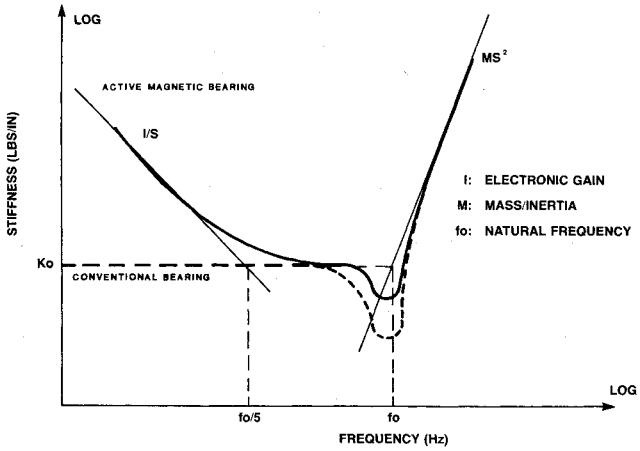

Fig. 14 Typical stiffness curve for active magnetic bearing.

Table 6 Air bearing vs magnetic bearing

Characteristic	Air bearing	Magnetic bearing
Wobble	~0.5 arcsec	0.04–0.02 arcsec
Orthogonality	~1 arcsec (not adjustable)	0.01 arcsec regulated by servo
Friction	Viscous 0.1 in.-lb/(rad/s)	0.8 in.-lb constant not dependent on rate
Stiffness	10×10^6 lb/in.	Function of disturbance frequency 0.1×10^6 lb/in. worst case
Reliability	High	Moderate due to complex control system
Simplicity of support system	Simple	Moderately complex

Angular Position Transducer

The error budget for the position transducer system is less than 0.02 arcsec. Several types of position transducers were evaluated during this study. Only two, however, were considered viable enough to warrant extensive investigation: the Inductosyn® (registered trademark of Farrand Inc., Valhalla, New York) and the absolute optical encoder. Transducer types considered either too developmental or not practical included the use of x rays passing through the lattice structure of a regular crystal and laser data disk technology. Inertial sensors were considered either too complicated or too inaccurate for for relative axis angular measurement.

A comparison of the Inductosyn with the absolute optical encoder was made using the following criteria:

1) Short-term stability (inherent noise level) of sensor and electronics must be well below the budgeted accuracy requirement.

2) Calibration via modeling systematic, repeatable errors should use minimal computation time and memory size.

3) Magnitude of repeatable errors must be small to minimize modeling errors.

4) Sensitivity of error to translation and undesired rotation must be small.

5) Sensitivity to EMI and RFI pickup should be small.

6) Periodic calibration requirements due to long-term drift should be low.

7) Cost should be minimized.

The rotary Inductosyn is a well-known absolute position transducer used in most of the inertial guidance test tables built by Contraves Goerz Corporation. The device uses the relationship between mutual (rotor-to-stator) inductance

Table 7 Comparison of Inductosyn and optical encoder

Criteria	Inductosyn	Optical encoder
Short-term stability (arcsec rms)	0.01	0.005
Systematic error magnitude (arcsec peak)	1 arcsec	1 arcsec
Modelability/calibration	Compact formula (small memory–high computation), possible to calibrate to within long-term stability of 0.001 arcsec peak	Point-by-point large memory, 0.05 arcsec peak without additional calibration
Sensitivity to translation/orientation	High	Low
Periodic calibration requirements	Low	High
Sensitivity to EMI/RFI	High	Moderate
Cost	Low	High

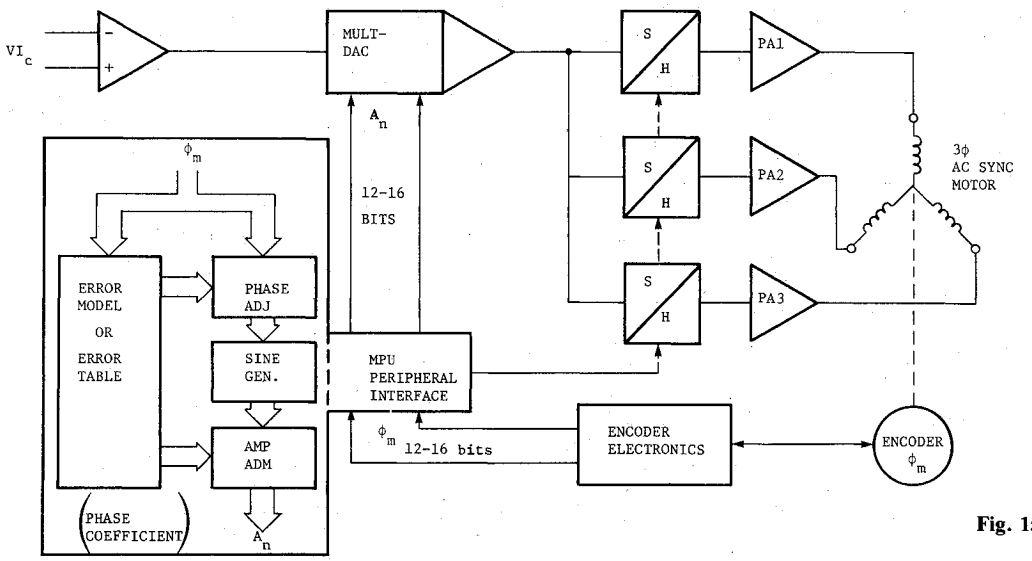

Fig. 15 ac synchronous drive system.

variations and relative angle of the rotor and stator similar to an ordinary two-phase resolver. An important difference between the resolver and Inductosyn is that the latter is a multispeed device, usually 360 speed.

Short-term stability of the system is governed by the inherent thermal noise of the windings and the wide-band noise produced or received by the drive electronics. The drive electronic noise is more than an order of magnitude larger than the inherent thermal noise; i.e., 0.01 arcsec rms for the drive noise and 0.0003 arcsec rms for the thermal noise. The repeatable (i.e., calibratable) errors of the Inductosyn come mainly from two sources: 1) distortion and balance errors in the electronic drive system and geometrical variations, or 2) undesired mechanical motion of the rotor and stator plates. The errors introduced by both error sources are typically on the order of 0.5 arcsec each. These errors may be reduced via calibration; however, they must be reduced to the point where variations in error magnitude due to temperature, component aging, etc., are not a factor in overall accuracy.

The Inductosyn error can be modeled[1] by

$$\text{Error } (\theta) = \left[\sum_{k=1}^{16} A_k \sin k\theta + B_k \cos k\theta\right] + \left[\sum_{m=1}^{4} C_m \sin nm\theta + D_m \cos nm\theta\right] \quad (10)$$

where n = Inductosyn speed.

For a given Inductosyn system, the coefficients of this equation will vary only as a function of the long-term stability of the plates. Long-term stability has been measured to be on the order of 0.001 arcsec peak. Only the first and sixteenth harmonics in the first factor and the nth, $2n$th, and $4n$th harmonics in the second factor of Eq. (10) dominate the error equations.

A conceptual design of a 25-bit (0.0386-arcsec resolution) absolute optical encoder was evaluated during the study. The primary encoder data are contained in the form of 18 binary optical patterns arrayed in concentric tracks. The reference data tracks, which provide the basic information pertaining to accuracy and resolution, contain 2^{16} line pairs (2^{17} bits) placed around the circumference of a 13-in.-diam glass disk. The data from this track are subsequently interpolated by a factor of 256 bits per bit to yield a final output of 2^{25} bits per revolution. The readout for all tracks uses an optical system containing light-emitting diodes, collimating lenses, reticle with slit pattern on the same pitch as the disk track, the disk, and photo-sensitive diodes. Drive electronics, including the interpolating memory, convert the output of the photodiodes to the 25-bit binary word representing angular position.

The systematic error (i.e., the sum of all error harmonics) of the reference data track is on the order of 1 arcsec peak. This may be calibrated through the use of multiple heads; with 32 heads spaced uniformly around the disk, the systematic error can be reduced to less than 0.05 arcsec peak.

Table 8 Comparison of ac synchronous and induction motors

Attribute	ac synchronous surface wound	ac synchronous ironless	ac induction laminated with copper	ac induction ironless-drag cup
Cogging torque	Low 0.005% of command	Low 0	Low 0.005% of command	Low 0
Ripple torque	Low 0.01% of command[a]	Low 0.01% of command[a]	Low 0.05% of command	Low 0.01% of command
Continuous torque performance	High	Low	High	Low
Maturity of motor technology	High	Low	High	Moderate
Maturity of drive technology	Moderate	Moderate	Moderate	Low
Intrinsic (vs calibrated) performance	Low	Low	High	High
Simplicity of drive	Low	Low	Low	Low

[a]Electronic commutation with systematic error correction.

Additional calibration of the encoder would most likely require point-by-point error correction; for a resolution of 10^{-5} deg, this requires a memory of 36 million words per axis. The broadband random error can be attributed to the photodiode noise, current to voltage transducer noise, summing and buffer amplifier noise, and A-to-D converter quantization. The quantization noise is by far the largest, with an rms value of approximately 0.005 arcsec.

Table 7 gives a general comparison of the two transducer systems. The accuracy of either system is ultimately limited by its short-term stability, the calibration technique, and the reference used in the calibration. Two methods of calibration were investigated: the back-to-back transducer technique[2] and divided circle terchnique.[3,4] On the basis of published performance to date, the divided circle technique will produce an order-of-magnitude less inherent noise (i.e., ~0.008 arcsec rms noise level) than the back-to-back method, and could provide the necessary reference for calibration of the position transducer.

Table 9 Recommended system configuration

Component	Specification
Structure	
Base material	Granite
Material	CFRP
Configuration	Spherical shell
Support bearing	
Type	Active magnetic
Configuration	Two radial and two thrust bearings per axis
Position encoding system	
Angular position transducer	Inductosyn
Actuator system	ac induction motor with a laminated iron rotor and copper conducting sheet on the surface
Signal transmission	Roll rings

Torque Actuators

During the initial phase of the study, several candidate systems for precision torque actuation were considered. Only two general types, represented by several variations, were investigated further. These were the ac synchronous and ac induction-type electric motors and drives.

Systems incorporating hydraulic, pneumatic, or reaction-wheel technology were eliminated because of high seal friction torques, poor performance at low speed, and excessively complex drives and support systems. The self-commutated dc motor was eliminated because of its rather large, random, inherent torque variations that are not amenable to on-line modeling and cancellation techniques.

The criteria used to compare the final four ac motor and drives were: torque disturbance magnitude, continuous torque performance, intrinsic vs calibrated performance, maturity of motor and drive technology, and drive simplicity.

Ac synchronous motor and brushless dc motor are names for one and the same motor concept. This motor performs exactly like a dc permanent magnet motor in terms of its electromagnetic characteristics. However, field rotation (motor-communication) must be accomplished by the drive electronics. In order to orient the electromagnetic field in the motor, multiphase field windings are incorporated that require a power amplifier to sinusoidally excite each winding. Referring to Fig. 15, the ac synchronous drive requires absolute knowledge of the motor shaft position to orient the electromagnetic field. The amplitude of the electromagnetic field is modulated in proportion to the torque command. The angle of the field is maintained perpendicular to the permanent field of the magnets (rotor). This keeps the torque sensitivity at its peak regardless of shaft position, and minimizes the torque ripple due to commutation errors. A microprocessor can be added to provide real-time compensation of measured (modeled) systematic errors.

The polyphase ac induction motor is capable of continuous torque production through the four quadrants of torque/speed operation. The motor is excited with a balanced stator supply, and sets up a magnetic field that, as it rotates, induces a voltage in the conductive material of the motor. The frequency of the induced voltage is equal to the difference of the stator and rotor velocity. The torque produced is proportional to the induced voltage divided by the net rotor impedance at the induced frequency. The function of the ac induction motor drive is to produce a multiphase excitation (field rotation) in proportion to the magnitude and sign of the torque command. The drive scheme for the two-phase motor is shown in Fig. 16. An input differential amplifier is provided for isolation and common mode rejection, the torque linearizing circuit is typically a square-root function since the torque produced is

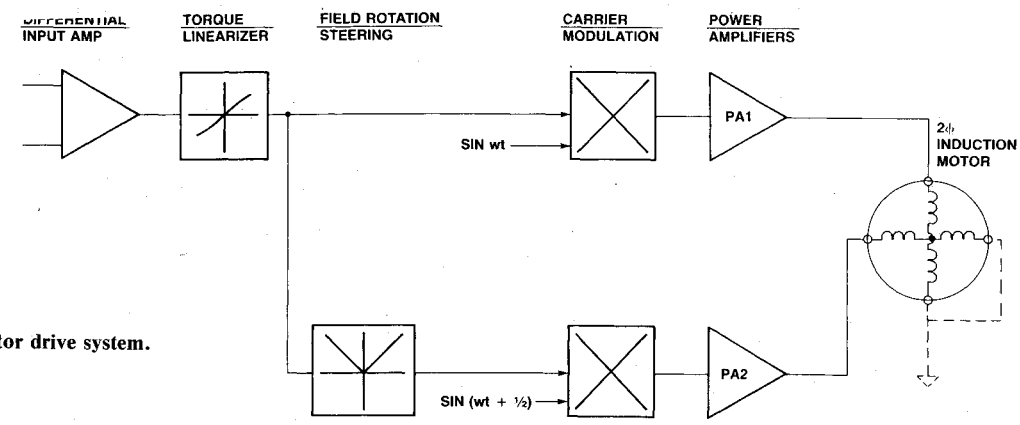

Fig. 16 Two-phase induction motor drive system.

Table 10 Required system performance

Item	Specification
Overall performance	
Overall pointing accuracy	0.1 arcsec
Rate stability (all axes measured over a 1-deg interval)	1 ppm
Axis freedom (all axes)	Continuous
Rate range (all axes)	±0.001–200 deg/s
Test package	
Size	12-in. cube
Weight	100 lb
Electrical service	100 lines minimum
Gimbal system	
Gimbal deflections (at axes intersection point)	<0.001 arcsec
Axis wobble	0.02 arcsec
Axes orthogonality	0.02 arcsec
Orientation	Outer axis horizontal
Encoding system	
Range	Continuous
Position accuracy (total per axis)	±0.02 arcsec
Broadband noise	0.01 arcsec rms
Position resolution	0.04 arcsec
Actuator system (including drive)	
Range	Continuous
Peak torque output	5 ft-lb
Torque ripple	$<15\times10^{-5}$ ft-lb peak
Broadband noise	$<5\times10^{-5}$ ft-lb rms
Control system	
Position mode	
Range	Continuous
Resolution	0.001 deg
Command noise	<0.012 arcsec rms
Rate mode	
Range	±0.001–200 deg/s
Resolution	0.001 deg/s
Command noise	$<3\times10^{-6}$ deg/s rms

essentially a result of the product of the drive currents. An absolute value circuit serves the function of sensing the sign of the torque command. By allowing only one phase to reverse sign, the direction of the field is reversed. The analog multipliers provide the modulation of the carrier, which may be fixed in frequency or varied as a function of the rotor speed. The power amplifiers are typically linear amplifiers with full power bandwidth beyond the maximum carrier frequency. Table 8 compares the four ac motors and drives.

Signal Transmission

The simulator must provide signal transmission to the test package on the innermost gimbal. This requirement, and the fact that all axes provide continuous rotation, immediately eliminate any sort of noncontinuous cable-wrapping devices. The viable candidates fall into two main catagories: noncontacting (radio, magnetic, and optical transmitter) and contacting [slip rings and Roll Rings (Roll Rings is a product developed and marketed by Sperry Flight Systems, Phoenix, Arizona)]. Although the noncontacting devices are very desirable from a friction-and-wear standpoint, they were eliminated from consideration due to the system complexity required to transmit power. Only the Roll Rings and slip rings were given further study.

Slip ring technology is relatively mature. It transfers signals or power to a rotating ring through a stationary brush-like device that pushes against the ring. Its biggest drawbacks are its somewhat high starting and running friction torques (30–50 and 15–25 in.-oz, respectively, per 100 lines). These drawbacks can be compensated for to some extent. The friction torque can be almost entirely eliminated by servoing the slip ring and using an optical coupling to control its position relative to the gimbal. The long-term signal degradation due to wear can be prevented with careful maintenance.

The Roll Ring assembly is a relatively new (within the last 10 years) item that replaces the brushes and rings of a slip ring with a rolling flexure element and two tracks. This reduces the friction torque significantly [typically less than 1 in.-oz (~0.005 ft-lb) per 100 lines]. Because the friction is reduced, the wear is also reduced and, thus, the undegraded life is increased. The operation of the device is limited to 100 rpm. This exceeds the rate range requirement and poses no problem.

Conclusion

The design study did not quantitatively address the environmental factors that might affect the pointing accuracy and rate stability of the test table. Some of the effects can be mitigated by proper design, such as shielding and filtering to reduce electromagnetic fields or the use of a seismically stable pier to reduce base disturbances. The symmetrical design of the table makes it impervious to balanced heat loads. Adequate room air conditioning and temperature control will be necessary only to keep thermal gradients across the table to less than the off-axis unbalanced heating case described earlier.

The final recommended system configuration, based on these investigations, is given in Table 9. In the case of the position transducer, both the Inductosyn and absolute optical encoder have the potential to meet the system requirements. The Inductosyn was chosen mainly on the basis of familiarity and cost. The same reasoning held true for the case of the actuator. Table 10 gives the overall system and subsystem performance requirements.

Acknowledgments

This work was completed for the U.S. Air Force under Contract F08635-83-C-0486, Central Inertial Guidance Test

Facility, Holloman Air Force Base, with R. Alexander as Project Manager.

The work reported in this paper on the active magnetic bearing was completed in cooperation with S2M (Societe De Mecanique Magetique), France; U.S. representative: Magnetic Bearings Inc., Radford, Virginia.

The work reported in this paper on the ultrahigh resolution optical encoders was completed in cooperation with Teledyne Gurley Corporation, Troy, New York.

References

[1]Brychatin, D.A. and Gol'dman, I. Ya., *Rotary Inductosyn General Information and Theory,* Energiya Publishing House, Leningrad, USSR, 1969, Chaps. 1-6.

[2]Hall, R.L., "Analysis Technique for Calibrating Angular Measuring Devices," AIAA Guidance and Control Conference, Aug. 1976.

[3]Hog, E., "Determination of Division Corrections," *Astronomische Nachrichten,* Vol. 286, 1961, pp. 65-78.

[4]Rafferty, T.J., "Heidenhein Glass Circles," Internal U.S. Naval Observatory Report.